



# Extreme Rarefaction of Solar Wind: A Study on Origin and Characteristics Using Ulysses Observations

Rajkumar Hajra<sup>1</sup> , Bruce T. Tsurutani<sup>2</sup> , Quanming Lu<sup>1</sup> , Lican Shan<sup>3</sup> , Aimin Du<sup>3</sup> , Rongsheng Wang<sup>1</sup> , San Lu<sup>1</sup> , and Xinliang Gao<sup>1</sup> 

<sup>1</sup> CAS Key Laboratory of Geospace Environment, School of Earth and Space Sciences, University of Science and Technology of China, Hefei, People's Republic of China; [rajkumarhajra@yahoo.co.in](mailto:rajkumarhajra@yahoo.co.in), [rhajra@ustc.edu.cn](mailto:rhajra@ustc.edu.cn)

<sup>2</sup> Retired, Pasadena, California, USA

<sup>3</sup> College of Earth and Planetary Sciences, University of Chinese Academy of Sciences, Beijing, People's Republic of China

Received 2023 May 29; revised 2023 August 4; accepted 2023 August 24; published 2023 September 26

## Abstract

From the Ulysses observation of the solar wind between the heliocentric distance  $r_h$  of  $\sim 1.0$  and  $\sim 5.4$  au during 1990–2009, we identified 53 intervals when the solar wind exhibited extreme rarefaction,  $\sim 2$  orders of magnitude decreases in the solar wind proton density  $N_p$  from their ambient values. These extremely low-density solar wind (ELDSW) events, characterized by an average (median)  $N_p$  of  $\sim 0.28 \pm 0.09$  ( $\sim 0.30$ )  $\text{cm}^{-3}$ , ram pressure of  $\sim 0.07 \pm 0.04$  ( $\sim 0.07$  nPa) and mass flux of  $\sim 166 \pm 84$  ( $\sim 159$ )  $10^{-22}$   $\text{kg cm}^{-2} \text{s}^{-1}$  all normalized to 1 au, have an average (median) duration of  $\sim 6.0 \pm 3.5$  days ( $\sim 5.5$  days), and radial extent of  $\sim 1.9 \pm 1.1$  au ( $\sim 1.9$  au). A clear hemispheric asymmetry is noted in their solar/interplanetary origin, with 70% being identified in the south hemisphere, and 30% in the north hemisphere of the heliosphere. About 23% of the events were encountered between  $r_h$  of 2.25 and 4 au, and 77% at  $r_h > 4$  au, indicating that these are not intrinsic properties of the Sun/solar corona but are created by the evolution of the solar wind with increasing radial distance from the Sun. The majority (49%) of the events occurred during magnetic clouds, 34% in solar wind high-speed stream (HSS) tails, 11% during the proper HSSs, and 6% during interplanetary sheaths. The identification of ELDSWs will have important consequences for their interaction with the magnetospheres of Jupiter and Saturn.

*Unified Astronomy Thesaurus concepts:* Solar wind (1534); Interplanetary medium (825); Interplanetary magnetic fields (824); Fast solar wind (1872); Solar coronal mass ejections (310); Corotating streams (314)

## 1. Introduction

The aim of this work is to identify and study extreme rarefaction of the solar wind and its associated solar/interplanetary phenomena. The present study is based on all solar wind measurements made by the Ulysses solar wind instrumentation during 1990–2009.

Knowledge of low interplanetary plasma densities is important for understanding solar wind interactions with planetary magnetospheres and comets, and potential expansion of those objects and the effects of processes within the objects. Regions of low interplanetary plasma densities can occur either by processes at the Sun (plus convection outward) or in interplanetary space by rarefaction (Sarabhai 1963; Parker 1965; Tsurutani et al. 2011a). There are only a few previously reported cases where the near-Earth solar wind density dropped to “abnormally” low values. These are:  $\sim 0.07 \text{ cm}^{-3}$  ion density measured by the International Sun–Earth Explorer (ISEE) spacecraft on 1979 November 22 (Gosling et al. 1982); an  $\sim 3.0\text{--}0.7 \text{ cm}^{-3}$  density decrease encountered by the Wind spacecraft on 1999 April 26 (Zhou et al. 2000; Fairfield et al. 2001);  $< 0.1 \text{ cm}^{-3}$  density encountered by the Wind, Advanced Composition Explorer (ACE), and Interplanetary Monitoring Platform 8 (IMP 8) spacecraft on 1999 May 10–11 (Usmanov et al. 2000, 2005; Fairfield et al. 2001; Smith et al. 2001); and  $< 0.1 \text{ cm}^{-3}$  density reported during 2002 May 24–25 (Chané et al. 2012, 2015). In addition to these near-Earth observations,

there are only two reports from a heliocentric distance  $> 1$  au: one on 1993 June 9–10 when Ulysses encountered abnormally low proton densities at  $\sim 4.6$  au (Gosling et al. 1994), and the other on 1996 May 1 when Ulysses measured a density drop of  $\sim 1$  order of magnitude at a heliocentric distance of  $\sim 4$  au (Riley et al. 1998). However, further analyses of the Ulysses magnetometer and ion composition data confirmed that the later event was due to an encounter with comet C/1996 B2 (Hyakutake; Gloeckler et al. 2000; Jones et al. 2000).

When a solar wind high-speed stream (HSS) encounters a slower stream, it creates a compression region where the solar wind density and pressure increase. These compression regions were named corotating interaction regions (CIRs; Smith & Wolfe 1976), not because the regions really corotated (the solar wind plasma comes out radially from the Sun), but because of the Sun’s rotation, the streams appear to corotate, very much like water from a spinning lawn sprinkler head. Other important references to this phenomenon, both before and after, can be found in the literature (Davis 1966; Davis et al. 1966; Belcher & Davis 1971; Gosling et al. 1978; Pizzo 1985; Tsurutani et al. 1995; Balogh et al. 1999; Echer et al. 2010; Hajra & Sunny 2022; Hajra et al. 2022; Sunny et al. 2023, and references therein). Behind HSSs, there can be a rarefaction region where the wind “stretches out,” leading to lower plasma densities and pressures. Thus, rarefaction regions can be created in the HSS trailing regions.

High-speed interplanetary coronal mass ejections (ICMEs) form fast-mode shocks and interplanetary sheaths (Kennel et al. 1985; Tsurutani & Lin 1985; Tsurutani et al. 1988). Similarly, rarefaction regions can occur in interplanetary sheaths and ICMEs as they expand radially outward. Actually, all interplanetary

phenomena may produce solar wind rarefaction, depending on their specific expansion effects with radial propagation. The slow solar wind (Belcher & Davis 1971; Gosling et al. 1981; Sheeley et al. 2009; Suess et al. 2009; Abbo et al. 2016; Tsurutani & Hajra 2022), heliospheric plasma sheet (HPS; Winterhalter et al. 1994) are all possible sources of the rarefaction.

To address the above issues, we have conducted statistical studies involving all solar wind measurements by Ulysses in order to identify and characterize intervals of extreme rarefaction of the solar wind. We will determine their statistical occurrences, their solar/interplanetary features, and/or their origins. Such a study has never been performed to date. Ulysses observations are most suitable for such a study, as Ulysses was the first probe that orbited the Sun out of the ecliptic plane and thus could measure the solar wind originating from equatorial to polar regions ( $0^\circ$  to  $\sim 80^\circ$ ) of the Sun. Its large heliocentric distance coverage ( $\sim 1.0$  to  $\sim 5.4$  au) is suitable for studying the solar wind heliospheric evolution. In addition, the  $\sim 19$  yr of Ulysses operation interval consists of all solar cycle phases, suitable to understand the solar cycle dependence of the results, if any.

## 2. Database and Analyses

The identification of the solar wind extreme rarefaction is based on hourly mean Ulysses data collected from NASA's COHOWeb<sup>4</sup>. All the solar wind plasma and interplanetary magnetic field (IMF) data collected from 1990 October 25 through 2009 June 30 are analyzed in this work. The IMF data are in the spacecraft-centered radial-tangential-normal (RTN) coordinate system, oriented with respect to the line connecting the Sun and the spacecraft. The radial axis is directed radially outward from the Sun through the spacecraft, and the tangential axis is parallel to the solar equatorial plane and is positive in the direction of the spacecraft's rotation around the Sun. The normal axis completes a right-handed system.

During this  $\sim 19$  yr period, the heliocentric distance  $r_h$  of the spacecraft varied between  $\sim 1.0$  and  $\sim 5.4$  au. Ulysses covered a large heliographic latitude range between  $\pm 80^\circ$ . The latitude is given in a Sun-centered heliographic inertial coordinate system, inertially fixed with respect to an  $x$ -axis directed along the intersection line of the ecliptic and solar equatorial planes. The  $z$ -axis is directed perpendicular and northward from the solar equator, and the  $y$ -axis completes the right-handed system.

The period of observation is characterized by solar cycle phases. For this purpose, the yearly mean  $F_{10.7}$  solar radio flux data are obtained from the Laboratory for Atmospheric and Space Physics (LASP) Interactive Solar Irradiance Data Center<sup>5</sup>.

The solar wind plasma and IMF parameters explored in this work are: solar wind proton density  $N_p$ , alpha density  $N_\alpha$ , alpha-to-proton density ratio  $N_\alpha/N_p$ , plasma speed  $V_{sw}$ , ram pressure  $P_{sw}$ , proton mass flux  $J_p$ , proton temperature  $T_p$ , IMF magnitude  $B_0$  and its components, plasma- $\beta$ , Alfvén wave speed  $V_A$ , magnetosonic wave speed  $V_{ms}$ , Alfvén Mach number  $M_A$ , and magnetosonic Mach number  $M_{ms}$ .  $J_p$  is computed as  $m_p N_p V_{sw}$ , where  $m_p$  is the proton mass.  $\beta$  is the ratio of the plasma pressure to the magnetic pressure.  $V_A$  is computed as  $B_0/\sqrt{\mu_0 \rho}$ ,  $V_{ms} = \sqrt{V_A^2 + V_s^2}$ , with  $V_s = \sqrt{5k_B(T_p + T_e)/3m_p}$ , where  $\mu_0$  is the free space permeability,  $\rho$  is the solar wind mass

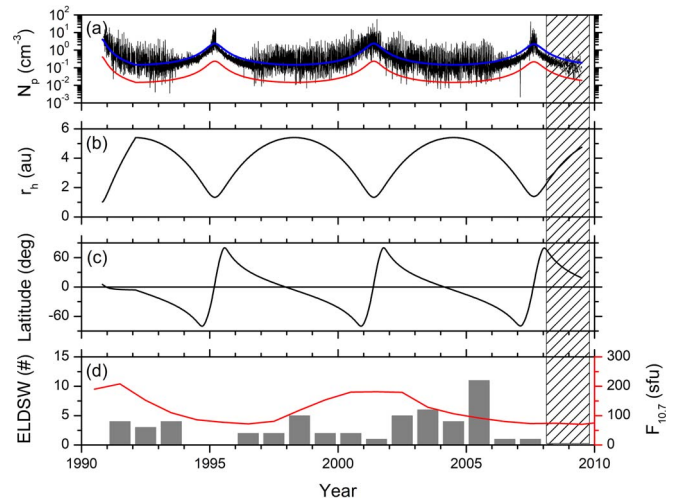


**Figure 1.** Solar wind plasma observations by Ulysses. From top to bottom, the panels show (a) proton density  $N_p$ ; (b) heliocentric distance  $r_h$ ; (c) heliographic latitude; (d) yearly numbers of ELDSW events (gray histograms, scale on the left), and yearly mean  $F_{10.7}$  solar radio flux (red curve, scale on the right). In panel (a), the blue line indicates  $4.21r_h^{-1.98}$ , the model fit to  $N_p$ , and the red line indicates 10% of the model values. See text for details. The vertical hatched region in 2009 and 2010 indicates a poor plasma data interval. The latter was not included in the analysis.

density,  $V_s$  is the sound speed,  $k_B$  is the Boltzmann constant, and  $T_e$  is the electron temperature.  $M_A$  and  $M_{ms}$  are defined as  $V_{sw}/V_A$  and  $V_{sw}/V_{ms}$ , respectively.

The magnetic field fluctuations are studied by variance analysis (Tsurutani et al. 1982, 2011b; Hajra et al. 2013, 2017) of the high (1 minute) resolution IMF data at time intervals of 5, 15, and 45 minutes. The variances are normalized by dividing them by the square of the IMF  $B_0$ . Nested normalized variances are computed from the 45 minute averages of the normalized variances.

Interplanetary discontinuities are explored to identify and characterize interplanetary shocks. Potential shocks are identified first manually by observations of the temporal variations of the 1 minute resolution solar wind plasma and IMF data. The abrupt increases in  $V_{sw}$  with simultaneous increases or decreases in  $N_p$ ,  $T_p$ , and  $B_0$  are identified as possible fast forward (FF) or fast reverse (FR) shocks, respectively. The plasma and magnetic field mixed-mode technique (Abraham-Shrauner 1972; Abraham-Shrauner & Yun 1976) is applied to determine the shock normal vector, its propagation angle ( $\theta_{Bn}$ ) with respect to the upstream IMF vector, the speed of propagation ( $V_{sh}$ ), and the magnetosonic Mach number ( $M_{ms}$ ) of the potential shocks (see Smith 1985; Tsurutani & Lin 1985; Tsurutani et al. 2011b; Hajra et al. 2016, 2020, 2023; Hajra & Tsurutani 2018; Hajra 2021, for details of the shock analysis). Only those with values  $M_{ms} > 1$  are confirmed as shocks, and those with  $M_{ms} < 1$  are identified as waves.

## 3. Results

### 3.1. Intervals of Extremely Low-density Solar Winds (ELDSWs)

Figure 1(a) shows all solar wind  $N_p$  measured by Ulysses.  $N_p$  exhibits an overall dependence on  $r_h$  (Figure 1(b)). To quantify this radial dependence,  $N_p$  data are separated into 0.25 au  $r_h$  bins. The mean  $N_p$  ( $\langle N_p \rangle$ ) was calculated for each 0.25 au bin.  $\langle N_p \rangle$  exhibits a power-law variation with  $r_h$ :  $\langle N_p \rangle = 4.21r_h^{-1.98}$  ( $\langle N_p \rangle$  is given in the unit of  $\text{cm}^{-3}$  and  $r_h$  in au). This

<sup>4</sup> <https://omniweb.gsfc.nasa.gov/coho>

<sup>5</sup> <https://lasp.colorado.edu/lisird/>

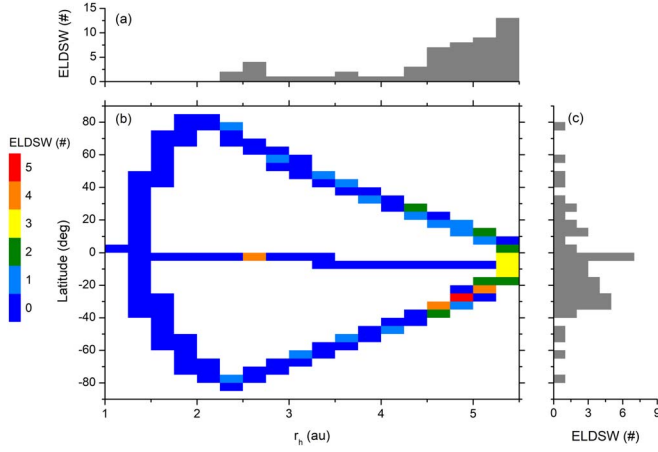


**Figure 2.** Radial and heliographic latitude dependences of the ELDSW events. (a) Radial distribution of ELDSWs. (b) ELDSW event number as a function of  $r_h$  (horizontal scale) and heliographic latitude (left-hand vertical scale). The ELDSW number corresponding to each color is given by the color bar on the left. (c) Latitudinal distribution of ELDSWs.

relationship is confirmed by a high regression coefficient ( $r$ ) of  $-0.99$ . The  $\langle N_p \rangle$  power-law fit is shown by the blue curve in Figure 1(a). The red curve represents 10% of  $\langle N_p \rangle$  and is shown for context. The latter value is taken as the arbitrary threshold level for the extreme rarefaction of the solar wind. We will call the solar wind with the minimum  $N_p$  value less than the threshold or less than 10%  $\langle N_p \rangle$  at a specific  $r_h$  as an “extremely low-density solar wind” (ELDSW) event. The ELDSW events represent significantly low  $N_p$  values compared to their radial average values. Following this method, 53 ELDSW events are identified from the Ulysses solar wind measurements. These are listed in Table A1 in the Appendix.

The yearly number of ELDSW events is shown as a histogram in Figure 1(d). In the same panel the yearly mean  $F_{10.7}$  solar radio flux is also plotted to indicate the solar cycle variation. The interval of study ranges from the maximum phase of solar cycle 22 to the minimum phase of the following cycle 23. The ELDSWs are found to occur mainly during the ascending and descending phases of the solar cycles.

The radial and heliographic latitude dependences of the ELDSW events are shown in Figure 2. From the latitude– $r_h$  contour plot (Figure 2(b)), it can be noted that from 1 to  $\sim 2$  au from the Sun, Ulysses covered the equatorial to polar regions of the Sun in both hemispheres. Ulysses did not encounter any ELDSW event in this region. With increasing  $r_h$ , the Ulysses coverage became narrower in lower latitudes. Among the 53 ELDSW events, only 23% were encountered between  $r_h$  of 2.25 and 4 au, and 77% were encountered at  $r_h > 4$  au (Figure 2(a)).

A clear hemispheric asymmetry can also be noted, with 70% being identified in the south hemisphere and only 30% in the north hemisphere of the heliosphere (Figure 2(c)). More interestingly, 85% of all cases were encountered between  $-40^\circ$  and  $+35^\circ$  latitudes—in the equatorial to midlatitude region. This also happens to be the largest radial distance.

From Figure 2, it is apparent that ELDSW events resulted from the radial evolution of solar wind at large  $r_h$  and low latitude, and not by features intrinsic to the Sun or to solar phenomena. This result is not totally unexpected but is shown here statistically for the first time.

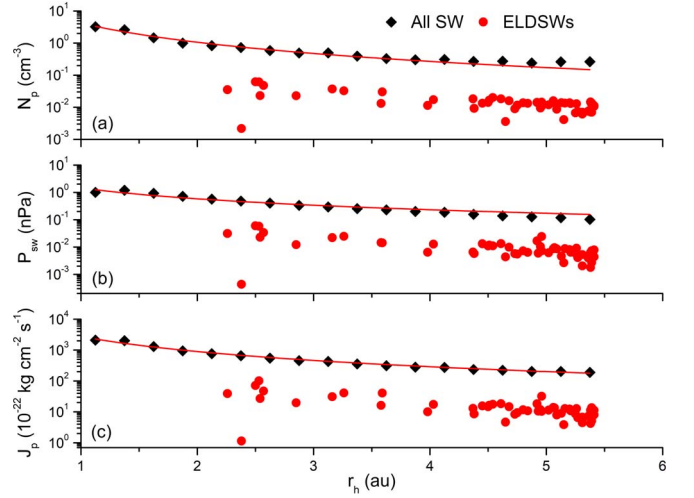


**Figure 3.** Radial variations of (a)  $N_p$ , (b)  $P_{sw}$ , and (c)  $J_p$ . Black diamonds and red dots correspond to all solar wind (SW) data and the ELDSW events, respectively. Red curves in each panel indicate power-law variations of the average parameters for all solar wind data.

For each of the ELDSW events, we estimated the minimum  $N_p$  value, and the  $P_{sw}$  and  $J_p$  values at the  $N_p$  minimum. Figure 3 shows the radial variations of ELDSW  $N_p$ ,  $P_{sw}$ , and  $J_p$  (red dots). These are compared with the radial variations of the average parameters for all solar wind data (black diamonds). With increasing  $r_h$ , the average  $N_p$ ,  $P_{sw}$ , and  $J_p$  exhibit power law decreases as  $r_h^{-1.98}$ ,  $r_h^{-1.33}$ , and  $r_h^{-1.63}$ , respectively (red curves). The radial relationships are confirmed by high anticorrelation coefficients  $r$  of  $-0.99$ ,  $-0.95$ , and  $-0.98$ , respectively. It can be clearly seen that the  $N_p$ ,  $P_{sw}$ , and  $J_p$  values for the ELDSW events are significantly lower than the radially average values for all solar wind data. The  $N_p$  minimum value varies from  $0.22 \times 10^{-2}$  to  $6.20 \times 10^{-2} \text{ cm}^{-3}$  for all ELDSW events, representing  $\sim 89\%$ – $99\%$  ( $\sim 2$  orders of magnitude) decreases from the ambient  $N_p$  values. Interestingly,  $N_p$  minimum values for all ELDSW events are highly correlated to  $P_{sw}$  (correlation coefficient  $r = 0.94$ ) and  $J_p$  ( $r = 0.95$ ).

Using the power-law radial variations (shown in Figure 3),  $N_p$ ,  $P_{sw}$ , and  $J_p$  are normalized to 1 au. The statistics of the normalized parameters are summarized in Table 1. The average values of the normalized  $N_p$  minimum ( $\sim 0.28 \text{ cm}^{-3}$ ),  $P_{sw}$  ( $\sim 0.07 \text{ nPa}$ ), and  $J_p$  ( $\sim 166 \times 10^{-22} \text{ kg cm}^{-2} \text{ s}^{-1}$ ) for all ELDSW events are approximately 1 order of magnitude lower than the average  $N_p$  ( $\sim 5.29 \text{ cm}^{-3}$ ),  $P_{sw}$  ( $\sim 1.24 \text{ nPa}$ ), and  $J_p$  ( $\sim 2775 \times 10^{-22} \text{ kg cm}^{-2} \text{ s}^{-1}$ ) for all solar wind data. While the  $1\sigma$  deviations from the mean values are significantly large for all solar wind data (96%–124%), the deviations are comparatively lower (32%–58%) for ELDSWs.

The durations of the ELDSW events are estimated from intervals where  $N_p$  is continuously less than the mean value. From the assumption that an ELDSW moves with the solar wind bulk velocity ( $V_{sw}$ ), the radial extent of the ELDSW is estimated as the area under the  $V_{sw}$  curve during the ELDSW interval (this is because  $V_{sw}$  is not constant during an ELDSW event). Statistical variations of ELDSW durations and radial extents are summarized in Table 1. Duration varies from a minimum value of  $\sim 4$  hr to a maximum value of  $\sim 12$  days, with an average duration of  $\sim 6$  days for all events. The radial extents of the ELDSW events vary from  $\sim 0.05$  to  $\sim 3.80$  au, with an average extent of  $\sim 1.93$  au for all events.

**Table 1**  
Statistical Characteristics of the ELDSW Events in Comparison to All Solar Wind Data

Parameter	ELDSW Events				All Solar Wind	
	Minimum	Maximum	Mean $\pm \sigma$	Median	Mean $\pm \sigma$	Median
$N_p$ minimum ( $\text{cm}^{-3}$ ) <sup>a</sup>	0.01	0.41	$0.28 \pm 0.09$	0.30	$5.29 \pm 6.56$	2.98
$P_{\text{sw}}$ (nPa) <sup>a</sup>	0.001	0.20	$0.07 \pm 0.04$	0.07	$1.24 \pm 1.18$	1.03
$J_p$ ( $10^{-22} \text{ kg cm}^{-2} \text{ s}^{-1}$ ) <sup>a</sup>	5	462	$166 \pm 84$	159	$2775 \pm 2927$	2044
Duration (days)	0.17	12.25	$5.99 \pm 3.48$	5.46	...	...
Size (au)	0.05	3.80	$1.94 \pm 1.10$	1.92	...	...

**Note.**

<sup>a</sup> Values are normalized to 1 au.

The above results clearly indicate that the ELDSW events are large-scale interplanetary structures, characterized by extremely low plasma densities, unusually low ram pressures, and low mass fluxes. The latter two parameter results simply follow the low plasma densities. To understand the associated large-scale interplanetary structures or the solar sources of the ELDSW events, solar wind plasma and IMF variations are explored in detail for each of the ELDSW events. Examples of ELDSW events associated with different large-scale interplanetary structures are shown in Section 3.2.

### 3.2. Interplanetary Structures

Figure 4 shows Ulysses measurements of solar wind plasma and IMFs during days 150–169 of year 1993. During this 20 days interval, the spacecraft was at  $r_h$  of 4.68 to 4.62 au, and heliographic latitude of  $-31.7$  to  $-33.0$ , in the south heliospheric hemisphere (Figure 4(h)). The solar wind variations indicate several discontinuities and large-scale structures.

The vertical solid lines at  $\sim 01:05$  UT on day 156, and at  $\sim 03:05$  UT on day 157 indicate abrupt increases in  $V_{\text{sw}}$  accompanied by simultaneous decreases in  $N_p$ ,  $P_{\text{sw}}$ ,  $T_p$ , and  $B_0$ —indicating FR shocks (FR<sub>156</sub>, FR<sub>157</sub>, respectively). The vertical dashed line at  $\sim 01:23$  UT on day 160 indicates an FF shock (FF<sub>160</sub>) characterized by abrupt increases in  $V_{\text{sw}}$ ,  $N_p$ ,  $P_{\text{sw}}$ ,  $T_p$ , and IMF  $B_0$ . The detailed characteristic parameters of the shocks are listed in Table 2.

The region of compressed plasma and IMFs from  $\sim 15:50$  UT on day 153 up to FR<sub>156</sub> is a CIR formed due to an interaction between a slow solar wind with  $V_{\text{sw}}$  of  $\sim 590 \text{ km s}^{-1}$  on days 150–152 and an HSS with  $V_{\text{sw}}$  of  $\sim 820 \text{ km s}^{-1}$  on days 157–159. The CIR is marked by a horizontal blue bar at the top and a cyan shading. While both the CIR and the HSS are characterized by large fluctuations in IMFs representing Alfvén waves, the wave amplitude is significantly enhanced during the CIR than during the HSS (Tsurutani et al. 1995). The latter is due to the larger IMF  $B_0$  within the CIR, while the relative field fluctuations remain essentially the same ( $\delta B/B_0 \sim 1$  to 2).

The impact of the FF<sub>160</sub> is a further compression of the IMFs and  $N_p$ , creating an interplanetary sheath up to  $\sim 22:00$  UT on day 160 (marked by a horizontal green bar at the top). The sheath is followed by smooth and slow rotating IMF components, and low  $T_p$  ( $\sim 5.6 \times 10^4 \text{ K}$ ) and low  $\beta$  ( $\sim 4.5 \times 10^{-2}$ ) up to  $\sim 22:00$  UT on day 164. These are the typical interplanetary signatures of a magnetic cloud (MC) that is part of an ICME (Burlaga et al. 1981; Klein & Burlaga 1982). The MC is marked by a horizontal red bar at the top and a magenta hatching.

While  $N_p$  falls below its radial mean value ( $\langle N_p \rangle$ , blue curve) during the HSS and the sheath,  $N_p$  is exceptionally low during the MC. It dropped below  $\langle N_p \rangle$  at  $\sim 07:00$  UT on day 160, and stayed below  $\langle N_p \rangle$  continuously up to  $\sim 16:00$  UT on day 164. The interval of  $\sim 4.38$  days is characterized by a minimum  $N_p$  of  $\sim 3.6 \times 10^{-3} \text{ cm}^{-3}$ , about a 99% decrease from the ambient  $N_p$  values. This represents an ELDSW event (marked by a horizontal bar in panel (b) and a gray shading). If the ELDSW is assumed to move with the solar wind bulk speed, it corresponds to a radial extent of  $\sim 1.87$  au.

The ELDSW event is characterized by lower  $N_\alpha$  ( $\sim 7.0 \times 10^{-5} \text{ cm}^{-3}$ ),  $N_\alpha/N_p$  ( $\sim 0.5 \times 10^{-2}$ ),  $P_{\text{sw}}$  ( $\sim 4.3 \times 10^{-3} \text{ nPa}$ ),  $J_p$  ( $\sim 4.7 \times 10^{-22} \text{ kg cm}^{-2} \text{ s}^{-1}$ ),  $M_A$  ( $\sim 2.56$ ), and  $M_{\text{ms}}$  ( $\sim 2.51$ ) compared to their values before the ELDSW impact.  $V_A$  ( $\sim 304 \text{ km s}^{-1}$ ) and  $V_{\text{ms}}$  ( $\sim 310 \text{ km s}^{-1}$ ) are enhanced during the ELDSW event.

Figure 5 shows the normalized variances of the IMF components for the ELDSW event shown in Figure 4. Interestingly, the ELDSW event is characterized by significant decreases in normalized variances compared to neighboring solar wind intervals. Low normalized variances indicate reductions in Alfvén wave activity during the ELDSW event (Tsurutani et al. 1982, 2011b; Hajra et al. 2013, 2017; Hajra & Tsurutani 2022).

Ulysses encountered multiple ELDSWs during days between 80 and 97 of year 1991 (Figure 6). The spacecraft was at  $r_h$  of 2.46–2.65 au, and heliographic latitude of  $-3.8$  to  $-4.1$  (Figure 6(h)), around the equatorial plane of the Sun. Analysis of the solar wind plasma and IMFs indicates multiple ICME impacts on days 82 through 92 (see Phillips et al. 1992 and Richardson 2014 for details of the ICME onsets and their characteristic parameters). An FF shock (FF<sub>082</sub>, vertical dashed line) is identified at  $\sim 15:34$  UT on day 82, computed to be propagating with speed  $V_{\text{sh}}$  of  $\sim 602 \text{ km s}^{-1}$  at an angle  $\theta_{\text{Bn}}$  of  $\sim 79^\circ$  with respect to the upstream IMF direction (Table 2). The FF<sub>082</sub> is followed by an interplanetary sheath (marked by a green bar at the top) up to  $\sim 08:10$  UT on day 83, characterized by compressed (enhanced) IMF  $B_0$  and  $N_p$ . From the smoothly rotating IMF components, enhanced  $B_0$ , and reduced  $\beta$ , we identified three consecutive MCs, from  $\sim 08:10$  UT on day 83 to  $\sim 00:43$  UT on day 85, from  $\sim 10:05$  UT on day 85 to  $\sim 05:31$  UT on day 87, and from  $\sim 07:41$  UT on day 87 to  $\sim 21:07$  UT on day 92. These are marked by red bars at the top and magenta hatchings.

Interestingly,  $N_p$  exhibits several large decreases during the MCs. In the intervals where  $N_p$  is continuously below radially mean  $N_p$  (blue curve in panel (b)) and attains a value less than 10% of the mean value (red curve), the ELDSW events are marked by gray shadings and horizontal black bars (Figure

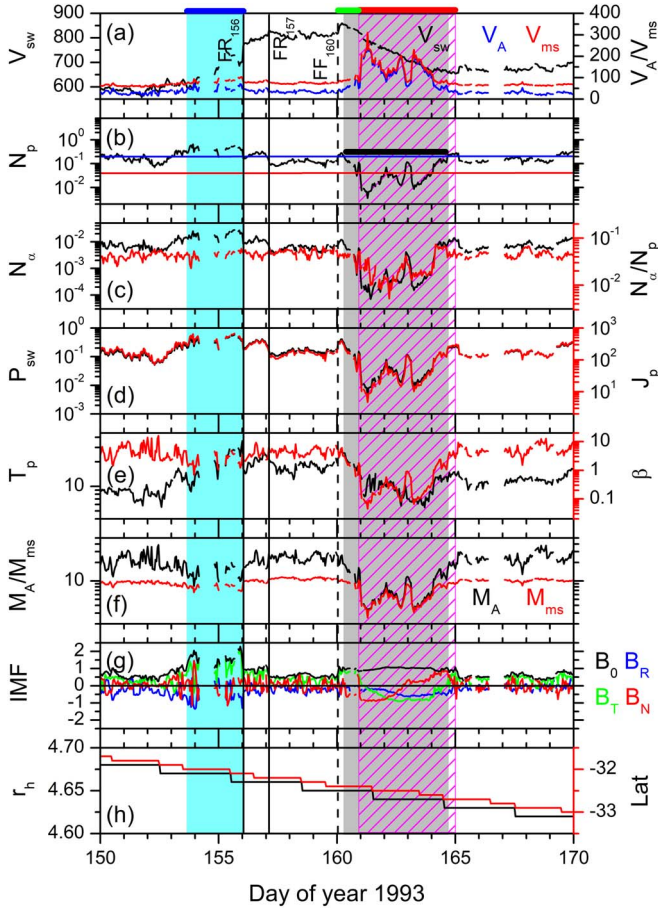


**Figure 4.** Solar wind variations on days 150–169 of year 1993. From top to bottom, the panels are (a)  $V_{sw}$  ( $\text{km s}^{-1}$ , black, scale on the left),  $V_A$  ( $\text{km s}^{-1}$ , blue, scale on the right) and  $V_{ms}$  ( $\text{km s}^{-1}$ , red, scale on the right); (b)  $N_p$  ( $\text{cm}^{-3}$ ), (c)  $N_\alpha$  ( $\text{cm}^{-3}$ , black, scale on the left) and  $N_\alpha/N_p$  (red, scale on the right); (d)  $P_{sw}$  (nPa, black, scale on the left) and  $J_p$  ( $10^{-22} \text{ kg cm}^{-2} \text{ s}^{-1}$ , red, scale on the right); (e)  $T_p$  (K, black, scale on the left) and  $\beta$  (red, scale on the right); (f)  $M_A$  (black) and  $M_{ms}$  (red); (g) IMF  $B_0$  (nT, black),  $B_R$  (nT, blue),  $B_T$  (nT, green), and  $B_N$  (nT, red); (h)  $r_h$  (au, black, scale on the left) and heliographic latitude (degree, red, scale on the right). Blue and red curves in panel (b) indicate the radially average  $N_p$  ( $\langle N_p \rangle$ ) and 10% level of  $\langle N_p \rangle$ , respectively. Vertical solid lines show interplanetary fast reverse (FR) shocks, and the vertical dashed line shows a fast forward (FF) shock. The blue horizontal bar at the top and cyan shading indicate a CIR, the green bar indicates an interplanetary sheath, and the red bar and magenta hatching indicate a magnetic cloud. An ELDSW event is marked by a horizontal bar in panel (b) and a gray shading.

6(c). Four ELDSW events are identified: from  $\sim 15:00$  UT on day 83 to  $\sim 07:00$  UT on day 84, from  $\sim 11:00$  UT on day 85 to  $\sim 07:00$  UT on day 87, from  $\sim 09:00$  UT on day 87 to  $\sim 21:00$  UT on day 88, and from  $\sim 23:02$  UT on day 88 to  $\sim 20:00$  UT on day 92. The ELDSW events are characterized by the minimum  $N_p$  values of  $\sim 6.2 \times 10^{-2}$ ,  $\sim 6.2 \times 10^{-2}$ ,  $\sim 2.3 \times 10^{-2}$  and  $\sim 4.8 \times 10^{-2} \text{ cm}^{-3}$ , presenting  $\sim 97\%$ ,  $\sim 95\%$ ,  $\sim 98\%$ , and  $\sim 95\%$  decreases from the ambient  $N_p$  values, respectively. Assuming the propagation of the ELDSW events with the solar wind bulk speeds, the events are found to have radial extents of  $\sim 0.25$ ,  $0.88$ ,  $0.62$ , and  $1.39$  au, respectively.

During the ELDSW events, the  $N_p$  minima are found to be well correlated with low  $N_\alpha$ ,  $N_\alpha/N_p$ ,  $P_{sw}$ , and  $J_p$ .

Variance analyses of the IMF components reveal reduced variances during the ELDSW events compared to neighboring

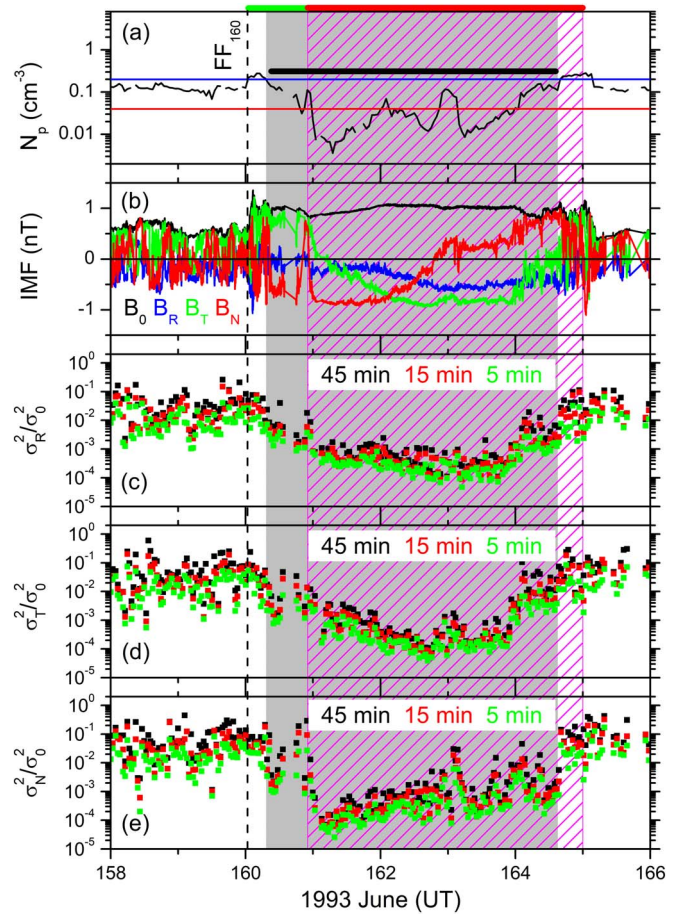


**Figure 5.** Variations of IMF on days 158–165 of year 1993. From top to bottom, panels are variations of (a)  $N_p$ ; (b) IMF  $B_0$  (black),  $B_R$  (blue),  $B_T$  (green), and  $B_N$  (red); normalized variances of (c)  $B_R$ , (d)  $B_T$  and (e)  $B_N$ . In panels (c)–(e), black, red, and green colors correspond to the normalized variances for 45 minutes, 15 minutes, and 5 minutes, respectively. The markings of interplanetary structures are repeated from Figure 4.

solar wind variances (not shown). This is consistent with the results obtained for the event shown in Figure 5.

In Figure 7, a long-duration ELDSW event is found to extend from an HSS proper through its tail. From the  $V_{sw}$  profile, a slow stream with  $V_{sw}$  of  $\sim 415$ – $461 \text{ km s}^{-1}$  can be identified during days 123–128 of 1998, and an HSS with  $V_{sw}$  of  $\sim 615$ – $640 \text{ km s}^{-1}$  on days 135–138, followed by gradually decreasing  $V_{sw}$  up to day 143. The CIR (marked by a blue bar at the top and a cyan shading), located between the slow stream and the HSS during days 130–135, is characterized by significant enhancements in  $N_p$  ( $\sim 1.9 \text{ cm}^{-3}$ ) and IMF  $B_0$  ( $\sim 3.66 \text{ nT}$ ), and fluctuations in the IMF components. During the CIR interval, there are significant increases in  $V_A$  ( $\sim 250 \text{ km s}^{-1}$ ) and  $V_{ms}$  ( $\sim 266 \text{ km s}^{-1}$ ), and consequent decreases in  $M_A$  ( $\sim 2.57$ ) and  $M_{ms}$  ( $\sim 2.41$ ). The leading edge of the CIR (at  $\sim 21:44$  UT on day 130) is characterized by sharp increases in  $V_{sw}$  ( $\sim 508$  to  $550 \text{ km s}^{-1}$ ),  $N_p$  ( $\sim 1.6 \times 10^{-1}$  to  $5.8 \times 10^{-1} \text{ cm}^{-3}$ ),  $P_{sw}$  ( $\sim 0.8 \times 10^{-1}$  to  $3.5 \times 10^{-1} \text{ nPa}$ ),  $T_p$  ( $\sim 5.8 \times 10^4$  to  $14.4 \times 10^4 \text{ K}$ ) and  $B_0$  ( $\sim 0.48$  to  $1.08 \text{ nT}$ )—an FF shock (FF<sub>130</sub>) with  $M_{ms}$  of  $\sim 1.31$ , propagating with  $V_{sh}$  of  $\sim 503 \text{ km s}^{-1}$  at  $\theta_{Bn}$  of  $\sim 56^\circ$  with respect to ambient IMF (Table 2). Another quasi-parallel ( $\theta_{Bn} \sim 28^\circ$ ) FF shock (FF<sub>132</sub>) with  $M_{ms}$  of  $\sim 2.78$  is identified at  $\sim 08:38$  UT on day 132, inside the CIR, propagating with  $V_{sh}$  of  $\sim 716 \text{ km s}^{-1}$ . At the CIR trailing edge, and during the entire HSS interval,

**Table 2**  
Characteristics of the Interplanetary Discontinuities Discussed in This Work

Year	DOY <sup>a</sup> /UT	$r_h$ (au)	Lat (deg)	$\theta_{Bn}$ (deg)	$V_{sh}$ (km s <sup>-1</sup> )	$M_{ms}$	Type <sup>b</sup>	Driver	References
1993	156/01:05	4.66	-32.1	82	372	2.56	FR <sub>156</sub>	CIR	Figure 4
1993	157/03:05	4.66	-32.2	74	652	1.10	FR <sub>157</sub>	CIR	Figure 4
1993	160/01:23	4.65	-32.4	54	784	1.72	FF <sub>160</sub>	ICME	Figure 4
1991	082/15:34	2.49	-3.8	79	602	1.78	FF <sub>082</sub>	ICME	Figure 6
1998	130/21:44	5.41	-7.3	56	503	1.31	FF <sub>130</sub>	CIR	Figure 7
1998	132/08:38	5.41	-7.3	28	716	2.78	FF <sub>132</sub>	CIR	Figure 7
1998	118/04:27	5.41	-6.6	53	297	1.18	FF <sub>118</sub>	ICME	Figure 8
1998	123/15:21	5.41	-6.9	83	516	1.71	FF <sub>123</sub>	ICME	Figure 8

**Notes.**

<sup>a</sup> DOY stands for day of year.

<sup>b</sup> The shocks are marked by their day of occurrence.

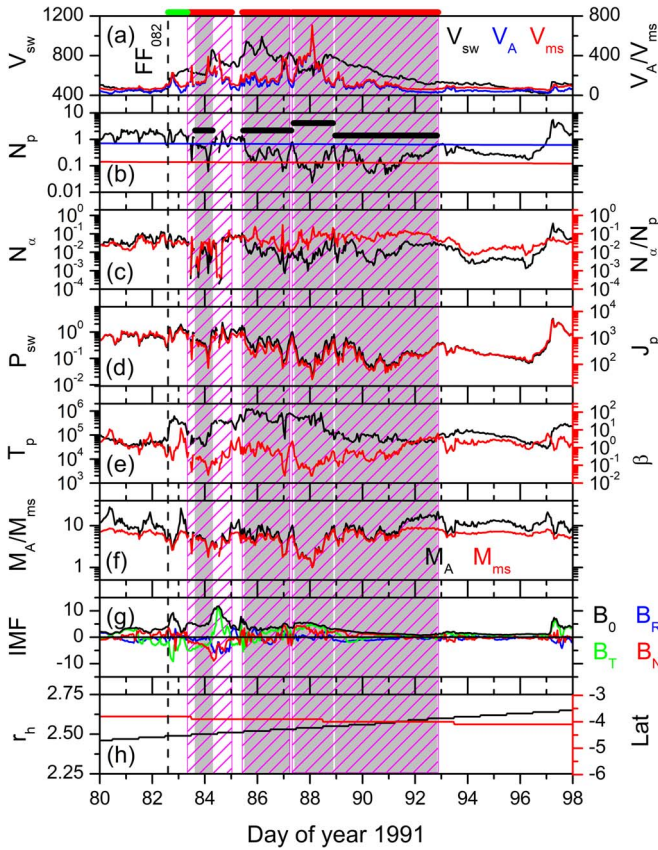


**Figure 6.** Solar wind variations on days 80–97 of year 1991. Panels are in the same format as in Figure 4. The vertical dashed line indicates an FF shock. An interplanetary sheath following the shock is marked by a horizontal green bar at the top. Three MC intervals are marked by horizontal red bars at the top and magenta hatchings. The ELDSW events are marked by gray shadings and horizontal black bars in panel (b).

$N_p$  decreases and remains below the radially mean  $N_p$  value (blue curve), reaching a minimum of  $\sim 1.1 \times 10^{-2} \text{ cm}^{-3}$  at  $\sim 20:00$  UT on day 136 (Figure 7(b)). The entire ELDSW interval (marked by gray shading and a horizontal bar in panel (b)), from  $\sim 16:00$  UT on day 135 to  $\sim 09:00$  UT on day 146, has a radial extent of  $\sim 3.05$  au.

The ELDSW event is characterized by lower  $N_\alpha$  ( $\sim 7.0 \times 10^{-5} \text{ cm}^{-3}$ ),  $N_\alpha/N_p$  ( $\sim 5.5 \times 10^{-3}$ ),  $P_{sw}$  ( $\sim 7.0 \times 10^{-3}$  nPa), and  $J_p$  ( $\sim 10.7 \times 10^{-22} \text{ kg cm}^{-2} \text{ s}^{-1}$ ) compared to their values before the event.  $T_p$  follows the  $V_{sw}$  variation pattern, which is

usual during an HSS. No significant variations are noted in  $\beta$ ,  $V_A$ ,  $V_{ms}$ ,  $M_A$ , and  $M_{ms}$  during the ELDSW event. From the variance analysis of the IMF components (not shown), the ELDSW event is again characterized by low variances compared to high-density intervals.

Figure 8 shows solar wind measurements during days 115–129 of year 1998, when Ulysses was at  $r_h = 5.41$  au, and heliographic latitude of  $-6^\circ.5$  to  $-7^\circ.2$  (Figure 8(h)). Analysis of the solar wind and IMF data indicates that the spacecraft encountered two interplanetary FF shocks (marked by vertical dashed lines) at  $\sim 04:27$  UT on day 118 (FF<sub>118</sub>) and at  $\sim 15:21$  UT on day 123 (FF<sub>123</sub>). The shock properties are given in Table 2. These shocks are associated with fast-moving ICMEs (see Richardson 2014). Following the shocks, the solar wind plasma and IMFs are compressed and heated in the interplanetary sheath.

Inside the sheath region,  $N_p$  sharply dropped at  $\sim 11:00$  UT on day 120. It is continuously below the radial mean value (blue curve) up to  $\sim 20:00$  UT on day 123, and reached a minimum value of  $\sim 1.1 \times 10^{-2} \text{ cm}^{-3}$  at  $\sim 02:00$  UT on day 122 (Figure 8(b)). The minimum  $N_p$  is significantly less than the 10% threshold level (red curve) of the mean  $N_p$ . The ELDSW interval of  $\sim 3.38$  days has an estimated radial extent of  $\sim 0.84$  au. The ELDSW event is characterized by lower  $N_\alpha$  ( $\sim 3.3 \times 10^{-4} \text{ cm}^{-3}$ ),  $P_{sw}$  ( $\sim 4.4 \times 10^{-3}$  nPa),  $J_p$  ( $\sim 8 \times 10^{-22} \text{ kg cm}^{-2} \text{ s}^{-1}$ ),  $M_A$  ( $\sim 4.7$ ), and  $M_{ms}$  ( $\sim 4.0$ ), but high  $T_p$  ( $\sim 12.2 \times 10^4$  K) compared to pre-event interval. While the sheath is characterized by highly fluctuating IMFs, the IMF component variances are significantly reduced during the ELDSW event (not shown).

### 3.3. Comparison among ELDSWs Associated with Different Drivers

The solar wind plasma and IMF variations have been explored in detail for each of the ELDSW events in order to understand the associated large-scale interplanetary structures and/or the solar sources of the ELDSW events (examples are shown in Section 3.2). Among the 53 ELDSW events encountered by Ulysses, the majority (49%) were identified during MCs, and 34% were observed at the trailing end of solar wind HSSs. The remainder of the ELDSWs were identified during the primary portion of HSSs (11%), and interplanetary sheaths (6%).

From these analyses, the consistent features of the ELDSW events are: extremely low  $N_p$ ,  $P_{sw}$ , and  $J_p$ , and low IMF variances. Other solar wind parameters, namely  $V_{sw}$ ,  $T_p$ ,  $\beta$ ,  $V_A$ ,

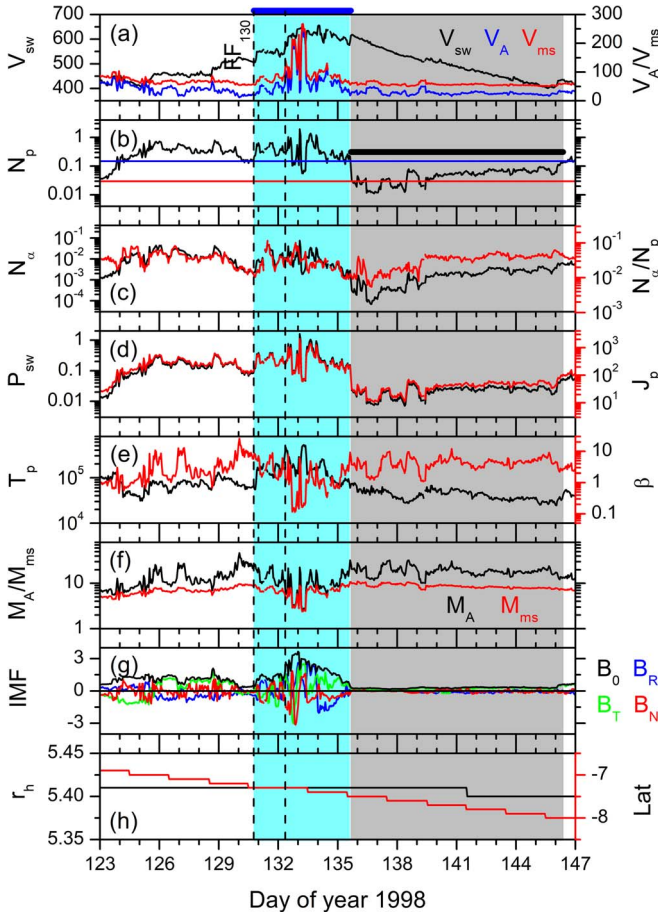


**Figure 7.** Solar wind variations on days 123–146 of year 1998. The format is the same as in Figure 4. Vertical dashed lines indicate FF shocks. A CIR following the shock is marked by a blue bar at the top and a cyan shading. The gray shading following the CIR is an HSS interval. A black bar in panel (b) shows an ELDSW event that is coincident with the HSS interval.

$V_{ms}$ ,  $M_A$ , and  $M_{ms}$ , exhibit varying patterns depending on the associated large-scale phenomena (MC/sheath/HSS proper/HSS tail). Statistical features of the ELDSW events associated with varying interplanetary structures/drivers are summarized in Table 3. While there is no apparent difference in the  $N_p$  minimum,  $P_{sw}$  and  $J_p$  values among ELDSWs associated with different drivers, durations, and radial extents of the events occurring at an HSS tail and inside an HSS proper are significantly larger ( $\sim 55\%$  and  $\sim 53\%$ , respectively) than those occurring during an interplanetary sheath and an MC.

#### 4. Summary and Discussion

From a detailed study of all solar wind data measured by the Ulysses spacecraft for  $\sim 19$  yr, we identified 53 intervals when the spacecraft encountered extremely low-density or ELDSW events. The main results can be summarized as follows:

1. The ELDSW events represent  $\sim 2$  orders of magnitude decreases in the solar wind  $N_p$ . They are characterized by an average (median)  $N_p$  of  $\sim 0.28 \pm 0.09$  ( $\sim 0.30$ )  $\text{cm}^{-3}$ ,  $P_{sw}$  of  $\sim 0.07 \pm 0.04$  ( $\sim 0.07$  nPa), and  $J_p$  of  $\sim 166 \pm 84$  ( $\sim 159$ )  $10^{-22} \text{ kg cm}^{-2} \text{ s}^{-1}$  all normalized to 1 au. The normalized IMF component variances are reduced, indicating attenuation of any Alfvénic wave activity during the ELDSW events.

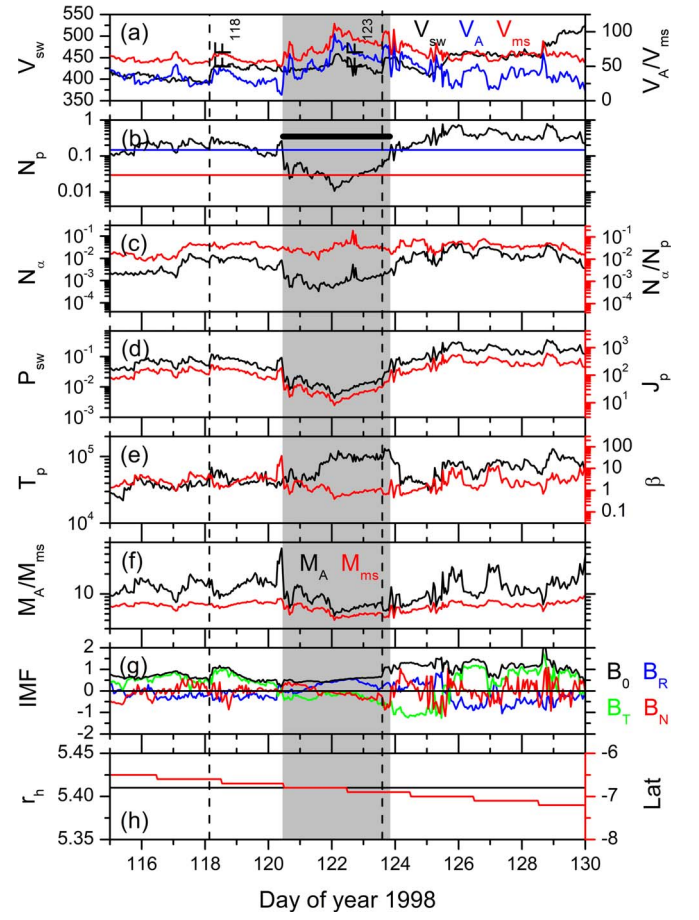


**Figure 8.** Solar wind variations on days 115–129 of year 1998. Panels are in the same format as in Figure 4. The vertical dashed lines indicate FF shocks. Gray shading and a horizontal black bar in panel (b) indicate an ELDSW event.

**Table 3**  
Comparison between ELDSW Events Driven by Different Drivers

Parameters	MC (26) <sup>a</sup> + Sheath (3) <sup>a</sup>		HSS tail (18) <sup>a</sup> + HSS proper (6) <sup>a</sup>	
	Mean $\pm \sigma$	Median	Mean $\pm \sigma$	Median
$N_p$ minimum ( $\text{cm}^{-3}$ ) <sup>b</sup>	$0.28 \pm 0.09$	0.30	$0.27 \pm 0.10$	0.30
$P_{sw}$ (nPa) <sup>b</sup>	$0.08 \pm 0.04$	0.07	$0.07 \pm 0.04$	0.06
$J_p$ ( $10^{-22} \text{ kg cm}^{-2} \text{ s}^{-1}$ ) <sup>b</sup>	$170 \pm 86$	148	$160 \pm 83$	164
Duration (days)	$3.87 \pm 2.65$	3.46	$8.56 \pm 2.51$	9.50
Size (au)	$1.29 \pm 0.89$	1.12	$2.72 \pm 0.78$	2.91

**Notes.**

<sup>a</sup> The number of ELDSW events.

<sup>b</sup> Values are normalized to 1 au.

2. The ELDSWs are large-scale interplanetary structures with an average (median) duration of  $\sim 6.0 \pm 3.5$  days ( $\sim 5.5$  days), and radial extent of  $\sim 1.9 \pm 1.1$  au ( $\sim 1.9$  au) for all events.
3. A clear heliospheric hemispheric asymmetry is noted in ELDSW occurrences. About 70% of the ELDSW events were detected in the south hemisphere, with the remaining 30% in the north hemisphere. About 23% of the events were encountered between  $r_h$  of 2.25 and 4 au, and the majority (77%) at  $r_h > 4$  au. These results indicate that the events are not intrinsic properties of the

Sun or the solar corona but are created by the solar wind evolution/expansion.

4. The majority (49%) of the events occurred within MCs, 34% at the solar wind HSS tails, 11% during the HSS proper, and 6% within interplanetary sheaths.
5. The ELDSW events occurring within an HSS tail or inside an HSS proper are found to be  $\sim 55\%$  longer in duration and  $\sim 53\%$  larger in radial extent than those occurring during an interplanetary sheath or an MC, on average.

Previous studies of extremely low-density solar wind at the Earth's orbit and beyond (Gosling et al. 1982, 1994; Usmanov et al. 2000, 2005; Zhou et al. 2000; Fairfield et al. 2001; Smith et al. 2001; Chané et al. 2012, 2015) have typically been only single case studies. Our present extensive, statistical, multiyear study effort reveals that extreme rarefaction of the solar wind may happen quite frequently both during the solar cycle ascending and descending phases at large heliocentric distances beyond  $\sim 4$  au from the Sun.

The average  $\sim 2$  au radial extent of ELDSWs indicates that they are large-scale interplanetary structures. The events are mainly recorded during MCs ( $\sim 49\%$ ) and within HSS tail regions ( $\sim 34\%$ ). A few of them are observed during the HSS proper intervals (11%) and the interplanetary sheaths (6%). While occurrences during sheaths and MCs are consistent with those behind fast-moving ICMEs, events during the HSS proper and tail regions are consistent with a rarefaction region with decreased plasma densities created in the trailing portion of an HSS (Sarabhai 1963; Parker 1965) due to a super-radial expansion of the solar wind (Tsurutani et al. 2011a). Radial evolution of corotating solar wind, formations of CIRs, and rarefaction of solar wind at the HSS tails in the interplanetary medium have been studied through numerical simulations as well as observations (e.g., Pizzo 1978; Pizzo & Gosling 1994; Gosling & Pizzo 1999; Hajra & Tsurutani 2022). Previous works have also suggested solar wind plasma rarefaction owing to radial expansions of ICMEs/MCs in the interplanetary medium (e.g., Gosling 1976; Burlaga et al. 1981; Klein & Burlaga 1982; Gosling et al. 1994; Hajra & Tsurutani 2022).

Another interesting result of this present work is the observed hemispheric asymmetry of the ELDSW occurrences. Previous Ulysses studies reported statistically significant south-to-north hemispheric asymmetries in solar wind plasma and IMF parameters, namely larger proton density, mass flux, ram pressure, and IMF magnitude in the southern hemisphere (e.g., McComas et al. 2000; Virtanen & Mursula 2010; Ebert et al. 2013), and a southward shift in the heliospheric current sheet (HCS; Virtanen & Mursula 2010; Wang & Robbrecht 2011;

Ebert et al. 2013). The enhanced solar wind parameters and their variabilities were attributed to higher solar activity levels and solar transients (ICMEs and HSSs) during the solar cycle declining phase when Ulysses was in the southern hemisphere than around the solar minimum when Ulysses was in the northern hemisphere. Thus, a larger occurrence of the ELDSW events in the south hemisphere than in the northern hemisphere (present finding) is consistent with the association of the events with the solar transients (ICMEs, HSSs) encountered in the south hemisphere.

While a solar wind rarefaction behind a fast ICME or at an HSS tailing region is well explained in general, why some of them become plasma extreme low-density regions, characterized by  $\sim 2$  orders of magnitude decreases, further from the Sun are not understood at this time. Further theoretical analyses and simulations will be useful in understanding dynamical evolution of these three ELDSW cases.

## 5. Final Comments

One surprise of this data analysis study is the potential impact that these ELDSW events will have on Space Weather for distant planets. As these events are mainly observed beyond  $\sim 4$  au from the Sun, enormous expansions of the magnetospheres of Jupiter (at  $\sim 5$  au) and Saturn (at  $\sim 10$  au) will take place with such ELDSWs impacts. These expansions will be more frequent, longer lasting, and more severe than cases at Earth.

## Acknowledgments

The work of R.H. is funded by the Chinese Academy of Sciences ‘‘Hundred Talents Program.’’ The work of Q.L. is supported by the National Science Foundation of China (NSFC) grant No. 42230201. The Ulysses data are collected from COHOWeb (<https://omniweb.gsfc.nasa.gov/coho/>). The  $F_{10.7}$  solar radio fluxes are obtained from the Laboratory for Atmospheric and Space Physics (LASP) Interactive Solar Irradiance Data Center (<https://lasp.colorado.edu/lisird/>). We would like to thank the reviewer for extremely valuable suggestions that substantially improved the manuscript.

## Appendix

Table A1 lists 53 ELDSW events encountered by Ulysses during 1990–2009, their encounter times by the spacecraft, location, interplanetary drives, and minimum  $N_p$  values. The value  $r_h$  and latitude correspond to the time of the  $N_p$  minimum identification.

**Table A1**  
The ELDSWs under This Study

Start Time	End Time	$r_h$ (au)	Latitude (deg)	$N_p$ Minimum ( $10^{-2}$ cm $^{-3}$ )	Interplanetary Structure
1991-03-24 15:00	1991-03-25 07:00	2.5	−3.9	6.2	MC
1991-03-26 11:00	1991-03-28 07:00	2.53	−3.9	6.2	MC
1991-03-28 09:00	1991-03-29 21:00	2.54	−3.9	2.3	MC
1991-03-29 23:02	1991-04-02 20:00	2.57	−4.0	4.8	MC
1992-08-28 01:00	1992-09-05 14:00	5.27	−16.4	0.7	HSS tail
1992-10-15 04:00	1992-10-24 18:00	5.2	−19.1	1.4	HSS tail
1992-11-13 22:00	1992-11-17 07:00	5.15	−20.3	0.4	MC
1993-02-17 06:00	1993-02-20 17:00	4.96	−25.6	1.1	MC
1993-04-06 18:00	1993-04-06 22:00	4.84	−28.4	1.3	MC
1993-06-09 07:00	1993-06-13 16:00	4.65	−32.4	0.4	MC

**Table A1**  
(Continued)

Start Time	End Time	$r_h$ (au)	Latitude (deg)	$N_p$ Minimum ( $10^{-2} \text{ cm}^{-3}$ )	Interplanetary Structure
1993-07-18 16:00	1993-07-23 19:00	4.5	-35.3	1.4	MC
1996-09-19 09:00	1996-09-30 00:00	4.38	25.8	0.9	HSS tail
1996-10-14 12:00	1996-10-20 06:00	4.45	24.2	1.3	MC
1997-01-02 22:00	1997-01-09 01:00	4.73	18.8	0.9	HSS tail
1997-01-27 10:00	1997-02-05 09:00	4.8	17.0	1.4	HSS tail
1998-04-30 11:00	1998-05-03 20:00	5.41	-6.8	1.1	Sheath
1998-05-15 16:00	1998-05-26 09:00	5.41	-7.5	1.1	HSS proper
1998-06-28 05:00	1998-06-28 14:00	5.39	-9.6	1.3	Sheath
1998-07-08 17:00	1998-07-17 10:00	5.39	-10.4	1.2	MC
1998-10-10 12:00	1998-10-15 11:00	5.31	-14.9	0.7	MC
1999-02-13 04:00	1999-02-15 08:00	5.13	-21.3	1.4	MC
1999-09-21 14:00	1999-09-30 03:00	4.54	-34.6	2.0	HSS proper
2000-04-30 07:00	2000-05-04 02:00	3.59	-53.2	3.0	MC
2000-07-10 03:00	2000-07-20 10:00	3.16	-62.4	3.7	MC
2001-11-11 07:00	2001-11-15 16:00	2.26	75.5	3.5	MC
2002-02-07 01:00	2002-02-11 10:00	2.85	58.1	2.3	HSS tail
2002-04-14 10:00	2002-04-24 02:00	3.26	48.3	3.3	HSS tail
2002-06-14 04:00	2002-06-16 18:00	3.58	41.3	1.3	MC
2002-08-28 04:00	2002-09-06 14:00	3.98	33.4	1.1	HSS tail
2002-12-06 05:00	2002-12-07 22:00	4.37	25.7	1.8	MC
2003-06-11 10:00	2003-06-16 08:00	4.95	13.5	0.9	MC
2003-07-03 11:00	2003-07-14 14:00	5.02	11.9	1.2	HSS tail
2003-07-31 19:00	2003-08-06 13:00	5.07	10.5	1.4	HSS tail
2003-09-18 13:00	2003-09-22 18:00	5.16	8.0	1.3	MC
2003-11-19 03:00	2003-11-29 11:00	5.25	4.8	0.7	MC
2003-12-30 03:00	2004-01-09 07:00	5.31	2.7	0.6	HSS proper
2004-02-28 21:00	2004-03-09 22:00	5.36	-0.6	0.8	HSS tail
2004-03-18 08:00	2004-03-20 12:00	5.38	-1.4	1.5	HSS tail
2004-04-22 03:00	2004-04-29 07:00	5.39	-3.3	0.7	HSS tail
2004-10-11 13:00	2004-10-12 02:00	5.38	-11.6	0.7	Sheath
2005-02-01 18:00	2005-02-09 00:00	5.26	-17.5	1.3	MC
2005-03-16 11:00	2005-03-19 22:00	5.21	-19.6	1.3	MC
2005-05-21 11:00	2005-05-23 20:00	5.09	-23.2	0.9	MC
2005-05-30 09:00	2005-06-09 21:00	5.06	-24.0	1.6	HSS proper
2005-07-18 01:00	2005-07-23 12:00	4.96	-26.5	1.4	HSS proper
2005-07-30 09:00	2005-08-02 11:00	4.93	-27.2	1.3	MC
2005-08-05 03:00	2005-08-08 17:00	4.92	-27.5	1.4	MC
2005-09-29 10:00	2005-10-09 17:00	4.75	-31.4	1.2	HSS tail
2005-10-24 07:00	2005-11-04 12:00	4.68	-32.9	1.6	HSS tail
2005-11-21 07:00	2005-12-03 13:00	4.61	-34.3	1.8	HSS proper
2005-12-13 20:00	2005-12-23 15:00	4.51	-36.3	1.7	HSS tail
2006-04-16 06:00	2006-04-22 19:00	4.03	-45.9	1.7	HSS tail
2007-02-04 15:00	2007-02-11 03:00	2.38	-79.7	0.2	HSS tail

**ORCID iDs**

Rajkumar Hajra  <https://orcid.org/0000-0003-0447-1531>  
Bruce T. Tsurutani  <https://orcid.org/0000-0002-0094-7224>  
Quanming Lu  <https://orcid.org/0000-0003-3041-2682>  
Lican Shan  <https://orcid.org/0000-0002-2354-9261>  
Aimin Du  <https://orcid.org/0000-0002-0525-7898>  
Rongsheng Wang  <https://orcid.org/0000-0002-9511-7660>  
San Lu  <https://orcid.org/0000-0003-2248-5072>  
Xinliang Gao  <https://orcid.org/0000-0003-0767-2267>

**References**

- Abbo, L., Ofman, L., Antiochos, S. K., et al. 2016, *SSRv*, 201, 55  
Abraham-Shrauner, B. 1972, *JGR*, 77, 736  
Abraham-Shrauner, B., & Yun, S. H. 1976, *JGR*, 81, 2097  
Balogh, A., Bothmer, V., Crooker, N., et al. 1999, *SSRv*, 89, 141  
Belcher, J. W., & Davis, L. 1971, *JGR*, 76, 3534  
Burlaga, L., Sittler, E., Mariani, F., & Schwenn, R. 1981, *JGR*, 86, 6673  
Chané, E., Raeder, J., Saur, J., et al. 2015, *JGRA*, 120, 8517  
Chané, E., Saur, J., Neubauer, F. M., Raeder, J., & Poedts, S. 2012, *JGRA*, 117, A09217  
Davis, J. L. 1966, in *The Solar Wind*, Proc. Conf., ed. R. J. J. Mackin & M. Neugebauer (Oxford: Pergamon), 147  
Davis, J. L., Smith, E. J., Coleman, J. P. J., & Sonett, C. P. 1966, in *The Solar Wind*, Proc. Conf., ed. R. J. J. Mackin & M. Neugebauer (Oxford: Pergamon), 35  
Ebert, R. W., Dayeh, M. A., Desai, M. I., McComas, D. J., & Pogorelov, N. V. 2013, *ApJ*, 768, 160  
Echer, E., Tsurutani, B. T., & Guarnieri, F. L. 2010, *AdSpR*, 45, 798  
Fairfield, D. H., Iver, H. C., Desch, M. D., et al. 2001, *JGR*, 106, 25361  
Gloeckler, G., Geiss, J., Schwadron, N. A., et al. 2000, *Natur*, 404, 576  
Gosling, J. T. 1976, in *Physics of Solar Planetary Environments*: Proc. Int. Symp. on Solar—Terrestrial Physics, ed. D. J. Williams (New York: Wiley)  
Gosling, J. T., Asbridge, J. R., Bame, S. J., & Feldman, W. C. 1978, *JGR*, 83, 1401  
Gosling, J. T., Asbridge, J. R., Bame, S. J., et al. 1982, *JGR*, 87, 239  
Gosling, J. T., Bame, S. J., McComas, D. J., et al. 1994, *GeoRL*, 21, 237

- Gosling, J. T., Borrini, G., Asbridge, J. R., et al. 1981, *JGR*, **86**, 5438
- Gosling, J. T., & Pizzo, V. J. 1999, *SSRv*, **89**, 21
- Hajra, R. 2021, *SoPh*, **296**, 33
- Hajra, R., Echer, E., Tsurutani, B. T., & Gonzalez, W. D. 2013, *JGRA*, **118**, 5626
- Hajra, R., Henri, P., Vallières, X., et al. 2017, *A&A*, **607**, A34
- Hajra, R., & Sunny, J. V. 2022, *SoPh*, **297**, 30
- Hajra, R., Sunny, J. V., Babu, M., & Nair, A. G. 2022, *SoPh*, **297**, 97
- Hajra, R., & Tsurutani, B. T. 2018, *ApJ*, **858**, 123
- Hajra, R., & Tsurutani, B. T. 2022, *ApJ*, **926**, 135
- Hajra, R., Tsurutani, B. T., Echer, E., Gonzalez, W. D., & Gjerloev, J. W. 2016, *JGRA*, **121**, 7805
- Hajra, R., Tsurutani, B. T., & Lakhina, G. S. 2020, *ApJ*, **899**, 3
- Hajra, R., Tsurutani, B. T., Lakhina, G. S., et al. 2023, *ApJ*, **951**, 75
- Jones, G., Balogh, A., & Horbury, T. 2000, *Natur*, **404**, 574
- Kennel, C. F., Edmiston, J. P., & Hada, T. 1985, A Quarter Century of Collisionless Shock Research (Washington, DC: AGU), 1
- Klein, L. W., & Burlaga, L. F. 1982, *JGR*, **87**, 613
- McComas, D. J., Barraclough, B. L., Funsten, H. O., et al. 2000, *JGR*, **105**, 10419
- Parker, E. N. 1965, *SSRv*, **4**, 666
- Phillips, J. L., Bame, S. J., Gosling, J. T., et al. 1992, *GeoRL*, **19**, 1239
- Pizzo, V. J. 1978, *JGR*, **83**, 5563
- Pizzo, V. J. 1985, in Collisionless Shocks in the Heliosphere: Reviews of Current Research, ed. B. T. Tsurutani & R. G. Stone (Washington, DC: AGU), 51
- Pizzo, V. J., & Gosling, J. T. 1994, *GeoRL*, **21**, 2063
- Richardson, I. G. 2014, *SoPh*, **289**, 3843
- Riley, P., Gosling, J. T., McComas, D. J., & Forsyth, R. J. 1998, *JGR*, **103**, 1933
- Sarabhai, V. 1963, *JGR*, **68**, 1555
- Sheeley, N. R., Lee, D. D. H., Casto, K. P., Wang, Y. M., & Rich, N. B. 2009, *ApJ*, **694**, 1471
- Smith, C. W., Mullan, D. J., Ness, N. F., Skoug, R. M., & Steinberg, J. 2001, *JGR*, **106**, 18625
- Smith, E. J. 1985, Interplanetary Shock Phenomena Beyond 1 au (Washington, DC: AGU), 69
- Smith, E. J., & Wolfe, J. H. 1976, *GeoRL*, **3**, 137
- Suess, S. T., Ko, Y. K., Von Steiger, R., & Moore, R. L. 2009, *JGRA*, **114**, A04103
- Sunny, J. V., Nair, A. G., Babu, M., & Hajra, R. 2023, *AdSpR*, **71**, 268
- Tsurutani, B. T., Echer, E., & Gonzalez, W. D. 2011a, *AnGeo*, **29**, 839
- Tsurutani, B. T., Gonzalez, W. D., Tang, F., Akasofu, S. I., & Smith, E. J. 1988, *JGR*, **93**, 8519
- Tsurutani, B. T., & Hajra, R. 2022, *ApJ*, **936**, 155
- Tsurutani, B. T., Ho, C. M., Arballo, J. K., Goldstein, B. E., & Balogh, A. 1995, *GeoRL*, **22**, 3397
- Tsurutani, B. T., Lakhina, G. S., Verkhoglyadova, O. P., et al. 2011b, *JASTP*, **73**, 5
- Tsurutani, B. T., & Lin, R. P. 1985, *JGR*, **90**, 1
- Tsurutani, B. T., Smith, E. J., Pyle, K. R., & Simpson, J. A. 1982, *JGR*, **87**, 7389
- Usmanov, A. V., Goldstein, M. L., & Farrell, W. M. 2000, *GeoRL*, **27**, 3765
- Usmanov, A. V., Goldstein, M. L., Ogilvie, K. W., Farrell, W. M., & Lawrence, G. R. 2005, *JGRA*, **110**, A01106
- Virtanen, I. I., & Mursula, K. 2010, *JGRA*, **115**, A09110
- Wang, Y. M., & Robbrecht, E. 2011, *ApJ*, **736**, 136
- Winterhalter, D. E., Smith, E. J., Burton, M. E., Murphy, N., & McComas, D. J. 1994, *JGR*, **99**, 6667
- Zhou, X., Tsurutani, B. T., & Gonzalez, W. D. 2000, *GeoRL*, **27**, 4025